

TEMPORAL EVOLUTION OF THE SCATTERING POLARIZATION OF THE CA II IR TRIPLET IN HYDRODYNAMICAL MODELS OF THE SOLAR CHROMOSPHERE.

E.S. CARLIN¹, A. ASENSIO RAMOS^{1,2}, J. TRUJILLO BUENO^{1,2,3}

Draft version November 16, 2018

ABSTRACT

Velocity gradients in a stellar atmospheric plasma have an effect on the anisotropy of the radiation field that illuminates each point within the medium, and this may in principle influence the scattering line polarization that results from the induced atomic level polarization. Here we analyze the emergent linear polarization profiles of the Ca II infrared triplet after solving the radiative transfer problem of scattering polarization in time-dependent hydrodynamical models of the solar chromosphere, taking into account the effect of the plasma macroscopic velocity on the atomic level polarization. We discuss the influence that the velocity and temperature shocks in the considered chromospheric models have on the temporal evolution of the scattering polarization signals of the Ca II infrared lines, as well as on the temporally averaged profiles. Our results indicate that the increase of the linear polarization amplitudes caused by macroscopic velocity gradients may be significant in realistic situations. We also study the effect of the integration time, the micro-turbulent velocity and the photospheric dynamical conditions, and discuss the feasibility of observing with large-aperture telescopes the temporal variation of the scattering polarization profiles. Finally, we explore the possibility of using the differential Hanle effect in the IR triplet of Ca II with the intention of avoiding the characterization of the zero-field polarization to infer magnetic fields in dynamic situations.

Subject headings: Polarization - scattering - radiative transfer Sun: chromosphere Stars: atmospheres, shocks

1. INTRODUCTION

The chromosphere, the interface region between the photosphere and the corona, is a very important part of the solar atmosphere. It is the place where most of the non-thermal energy that creates the corona and solar wind is released, with a heating rate requirement that is between one and two orders of magnitude larger than in the corona. To infer the thermal, dynamic and magnetic structure of the solar chromosphere is thus a very important goal in astrophysics. For instance, it is believed that the dissipation of magnetic energy in the 10^6 K corona may be significantly modulated by the strength and structure of the magnetic field in the chromosphere (e.g., Parker 2007). However, “measuring” the chromospheric magnetic field is notoriously difficult (e.g., reviews by Casini & Landi Degl’Innocenti 2007; Harvey 2009; Trujillo Bueno 2010). While spectroscopic observations allow us to determine temperatures, flows and waves, they do not provide any quantitative information on the chromospheric magnetic field. To this end, we need to measure and interpret the polarization that some physical mechanisms introduce in chromospheric spectral lines. These mechanisms are the Zeeman effect, scattering processes and the Hanle effect.

The circular and linear polarization signals that the Zeeman effect can in principle produce in a spectral line are caused by the wavelength shifts between the π and σ transitions of the line, as a result of the Zeeman splitting induced by the presence of a magnetic

field. The amplitude of the circular polarization scales with the ratio, \mathcal{R} , between the Zeeman splitting and the Doppler line width. The amplitude of the linear polarization scales with \mathcal{R}^2 (see Landi Degl’Innocenti & Landolfi 2004). Outside sunspots (where $B \lesssim 100$ G at chromospheric heights) $\mathcal{R} \ll 1$, which explains why it is so difficult to detect the polarization of the Zeeman effect in a chromospheric line. Typically, only the circular polarization is detected, especially in long-wavelength chromospheric lines such as those of the IR triplet of Ca II (e.g., Trujillo Bueno 2010, figure 3). But the linear polarization observed in quiet regions of the solar chromosphere has practically nothing to do with the transverse Zeeman effect.

In weakly magnetized regions, the linear polarization of chromospheric lines is dominated by scattering processes. The physical origin of this polarization is the difference among the electronic populations of sublevels pertaining to the levels of the spectral line under consideration. This so-called atomic level polarization, which is caused by the anisotropic illumination of the atoms, produces selective emission and/or selective absorption of polarization components without the need of a magnetic field (e.g., Manso Sainz & Trujillo Bueno 2003b, 2010). The larger the anisotropy of the incident radiation field the larger the induced atomic level polarization and the larger the amplitude of the linear polarization of the emergent spectral line radiation. In an optically thick plasma like the solar atmosphere, the anisotropy of the radiation field depends mainly on the spatial distribution of the physical quantities that determine, at each point within the medium, the angular variation of the incident intensity. Great attention has been paid to the gradient of the source function (e.g., Trujillo Bueno 2001; Landi Degl’Innocenti & Landolfi 2004) but, in a highly

ecarlin@iac.es

¹Instituto de Astrofísica de Canarias, 38205, La Laguna, Tenerife, Spain

²Departamento de Astrofísica, Facultad de Física, Universidad de La Laguna, Tenerife, Spain

³Consejo Superior de Investigaciones Científicas, Spain

dynamic medium like the solar chromosphere, the gradients of the macroscopic velocity of the plasma may also play an important role (Carlin et al. 2012, and references therein). In fact, in Carlin et al. (2012, hereafter Paper I) we showed that it can affect significantly the scattering polarization of the IR triplet of Ca II. Our arguments were based on radiative transfer calculations in a semi-empirical model of the solar atmosphere, after introducing ad-hoc velocity gradients and comparing the computed Q/I profiles with those corresponding to the static case. Given the diagnostic potential of the Ca II IR triplet for exploring the magnetism of the solar chromosphere (e.g., Manso Sainz & Trujillo Bueno 2010; De la Cruz Rodriguez et al. 2012), and the fact that the region where such chromospheric lines originate may be affected by vigorous and repetitive shock waves (e.g., Carlsson & Stein 1997), it is necessary to investigate the radiative transfer problem of scattering polarization in the Ca II IR triplet using dynamical, time-dependent atmospheric models of the solar chromosphere. In this paper, we show the results of such investigation.

2. DESCRIPTION OF THE PROBLEM AND THE RESOLUTION PROCEDURE.

We have carried out radiative transfer calculations of the linear polarization produced by scattering in the Ca II infrared (IR) triplet. The polarization is produced by the atomic level polarization that results from anisotropic radiation pumping in the hydrodynamical (HD) models of solar chromospheric dynamics described in Carlsson & Stein (1997, 2002).

We used two time series of snapshots from the above-mentioned radiation HD simulations, each one lasting about 3600 s and showing the upward propagation of acoustic wave trains growing in amplitude with height until they eventually produce shocks. The first one corresponds to a relatively strong photospheric disturbance showing well-developed cool phases and pronounced hot zones at chromospheric heights (see Carlsson & Stein, 1997; we refer to this as the strongly dynamic case). The second simulation corresponds to a less intense photospheric disturbance (see Carlsson & Stein, 2002; we refer to this as the weakly dynamic case). Thus, the thermodynamical evolution of the atmosphere (including the chromosphere and the transition region) is driven by the bottom boundary condition that is imposed on the velocity. This realistic boundary condition is extracted from the measured Doppler shifts in the Fe I line at 3966.8 Å. Our description focuses mainly on the strongly dynamic case, but in Sec. 4.5 we compare the results with those corresponding to the weakly dynamic case.

To characterize the simulations we can use the following quantities. In terms of the velocity gradients, and using units related to a representative scale height ⁴ $\mathcal{H} = 275$ km, the temporal average of the maximum velocity gradient along the atmosphere is $40 \text{ km} \cdot \text{s}^{-1}$ per scale height (or $145 \text{ m} \cdot \text{s}^{-1} \text{ km}^{-1}$) in the strongly dynamic case

⁴ A scale height can be defined as the typical distance over which atmospheric magnitudes such as the density vary an order of magnitude. But the scale height is not a fixed quantity in a time-dependent model that contains important temporal variations in those magnitudes. For this reason we have defined an averaged scale height as the *representative* value used for the characterization of the velocity gradients.

and $13 \text{ km} \cdot \text{s}^{-1}$ per scale height (or $47 \text{ m} \cdot \text{s}^{-1} \text{ km}^{-1}$) in the weakly dynamic case. Likewise, the temporal average of the minimum of temperature in the atmosphere is 3976 K in the strongly dynamic case, and 4292 K in the weakly dynamic case.

At each time step of the HD simulation under consideration we use the corresponding one-dimensional stratifications of the vertical velocity, temperature and density to compute the emergent $I(\lambda)$ and $Q(\lambda)$ profiles through the application of the multilevel radiative transfer code of Manso Sainz & Trujillo Bueno (2003a, 2010), after the generalization to the non-static case described in Carlin et al. (2012). Specifically, we have solved jointly the radiative transfer (RT) equations for the Stokes I and Q parameters and the statistical equilibrium equations (SEE) for the atomic populations of each energy level and the population imbalances among its magnetic energy sublevels (equivalently, the multipolar tensor components of the atomic density matrix, $\rho_0^K(J_i)$, with J_i the angular momentum of each level i). This is the NLTE radiative transfer problem of the second kind (see sections 7.2 and 7.13 in Landi Degl'Innocenti & Landolfi 2004)). Once the self-consistent solution of such equations is found at each height in the atmospheric model under consideration, we compute the coefficients of the emission vector and of the propagation matrix (see section 2.2 of Paper I) and solve the RT equations for a line of sight (LOS) with $\mu = 0.1$, where μ is the cosine of the heliocentric angle. This LOS has been chosen in order to simulate a close to the limb observation, such as that shown in figure 13 of Stenflo et al. (2000). To account for the macroscopic motions, we have introduced the Doppler effect in the calculation of the absorption and emission profiles for each wavelength and ray direction (Paper I). The influence of the Doppler effect on the SEE appears directly because the radiative rates depend on the radiation field tensor components. Likewise, the RTE is affected because the Doppler effect modifies the elements of the propagation matrix and of the emission vector.

Given that the computations reported here are carried out in plane-parallel atmospheric models, it is necessary to introduce a micro-turbulent velocity, that accounts for the Doppler shifts (inducing an effective line broadening) produced by moving fluid elements below the resolution element. In order to estimate a suitable value (assumed constant with height), we have calculated the emergent intensities at disk center and compared them with those of the solar Kitt Peak FTS Spectral Atlas (Kurucz et al. 1984). A good agreement is obtained with 3.5 km s^{-1} .

3. DESCRIPTION AND CHARACTERIZATION OF THE RESULTS.

A standard Fourier analysis of the atmosphere model shows that it acts as a pass-band filter for the multifrequency sound waves generated in the lower boundary. The result is that the predominating periods at chromospheric heights and higher are around three minutes (Carlsson & Stein 1997). For practical reasons we divided the temporal evolution in 3-min intervals so that the beginning of each interval coincides with the moment in which the shock front in temperature and velocity is the sharpest in each interval (vertical lines in figures with temporal axis, like Fig. 1). Given the power of the 3-min

waves, this division turns out to be “natural” and can be used to mark the most interesting events we see in the emergent polarization.

Inside each three-minute cycle we distinguish between *compression* and *expansion* phases. They can be easily identified following the height at which $\tau_{\nu_0}^{los} = 1$, i.e., where the optical depth at line center (ν_0) along the LOS equals unity (upper panel of Fig. 1). This quantity is a good marker of the shock fronts when they cross heights between 1 and 2 Mm. It is because the steep changes in opacity inside the shocks forces the $\tau = 1$ region to remain comprised within them. The line transitions at 8542 Å and 8662 Å (green and red lines in the upper panel of Fig. 1) follow a clearer periodic pattern because they form higher, where less frequency components of the velocity waves can arrive. Compression phases begin when plasma falls down from upper layers ($\tau_{8542}^{los} = 1$ and $\tau_{8662}^{los} = 1$ decrease in top panel of Fig. 1), while simultaneously a new upward propagating wave emerges amplified into the chromosphere. At the end of this stage a shock wave is completely developed and the $\tau_{\nu_0}^{los} = 1$ position is close to ~ 1200 km for the three IR lines. The shock waves so created start always in such region between 1 and 1.5 Mm⁵. After that, during what we term expansion phase (heights for $\tau_{8542}^{los} = 1$ and $\tau_{8662}^{los} = 1$ arising in top panel of Fig. 1), the shock fronts travel upward increasing the plasma velocities as they encounter lower densities.

Figure 1 also shows the time evolution of other quantities during the first 2000 s after the initial transient. In the second row, the location and value of the temperature minimum are displayed, showing a clear correspondence with expansion and contraction phases. In the third row, we show the ensuing variation of $(Q/I)_{pp}$, defined as the peak-to-peak difference of the Q/I profile for each spectral line. It is a measure of the linear polarization signal contrast that was used in Paper I to characterize the polarization amplitude and discriminate their variations with respect to static cases. In each cycle we see an amplification of $(Q/I)_{pp}$ occurring at expansion phases and an usually larger amplification during contraction phases. Finally, the time evolution of the emergent $Q(\lambda)/I(\lambda)$ profile for the 8542 Å line is illustrated in the lower panel (the vertical axis shows 0.6 Å around the rest wavelength of the line). Here, we observe two distinct areas showing amplifications inside each three-minute cycle. The first amplification is blue-shifted, because it happens in an atmospheric expansion phase (plasma moving towards the observer). It is weaker than the second amplification, which is red-shifted and occurs during the compression phase (plasma moving down in the atmosphere). This indicates that the compression phase is more efficient producing a polarization amplification than the expansion one. The reason is that during compression we have stronger velocity and temperature gradients along the main regions of formation. Following the results of Paper I, the larger the gradient, the larger the enhancement of the linear polarization signal. The behaviour is similar in the other transitions.

⁵ It is in this range of heights where the Ca II IR triplet forms in typical semi-empirical models

There is a clear correspondence between the maximum value of the temperature minimum (hot-chromosphere time-steps) and the largest peaks of the $(Q/I)_{pp}$ signal, taking place just before the maximum contraction (dotted vertical lines). As the atmosphere is compressed, the temperature increases at chromospheric heights and the resulting gradient of the source function produces an increase of the radiation field anisotropy in the upper layers. This directly leads to an enhanced emergent linear polarization signal. On the contrary, in cold-chromosphere models the expansion reaches its maximum and $(Q/I)_{pp}$ is near its minimum value.

Even in such complex situations, we still witness the already known effects of amplification (with respect to the static case), frequency shift and asymmetry in the linear polarization profiles due to dynamics. All of them have been already explained in Paper I, using the semi-empirical FAL-C model of Fontenla et al. (1993) with ad-hoc velocity stratifications. The enhancement is produced as a consequence of the velocity gradients and subsequent anisotropy enhancements. However, some differences exist from the experiments in semi-empirical models and the calculations presented in this paper. First, the velocity stratification in the HD models is, in general, non-monotonic and with a non-constant variation with height. Second, the maximum velocity gradients are located at shocks, with amplitudes that reach tens or even hundreds of meters per second per kilometer (as a comparison, in Paper I we dealt with velocity gradients between 0 and 20 m s⁻¹ km⁻¹). Third, as commented before, we have shocks in temperature that produce larger source function gradients and additional enhancement of the radiation anisotropy and of the linear polarization. Finally, these variations are usually concentrated in the formation regions of the triplet lines. All these mechanisms act together and enhance the linear polarization of the emergent radiation with amplification factors up to ~ 10 (in the 8498 Å line) and ~ 7 (in the 8542 Å and 8662 Å lines), for the instantaneous values of the Q/I amplitudes with respect to the static FAL-C case. However, if we consider temporal averages of the emergent Stokes profiles during long periods, we get amplification factors of about a factor of 2 (time-averaged Q/I amplitudes reach $\sim 1\%$ for 8542 Å and 8662 Å lines).

Summarizing, the temporal evolution of the polarization is driven by the temperature and velocity stratifications, that in turn are a result of the dynamical conditions set in the photosphere.

4. ANALYSIS AND DISCUSSION OF RESULTS.

4.1. *The effect of the velocity.*

A way of visualizing the effect of vertical velocity gradients on the emergent scattering polarization is to compare the evolution of the polarization profiles corresponding to both the static and non-static case. In the absence of velocities (lower row of Fig. 2), the maximum of the Q/I profiles is always located at $\lambda = \lambda_0$ (i.e., line center), and its temporal evolution presents a sawtooth shape. When the effect of velocities is included in the calculations (upper row of Fig. 2), the maximum of the Q/I signal is no longer located at the central wavelength and its temporal evolution assumes a different shape with two peaks every 3-min period (upper right panel). These

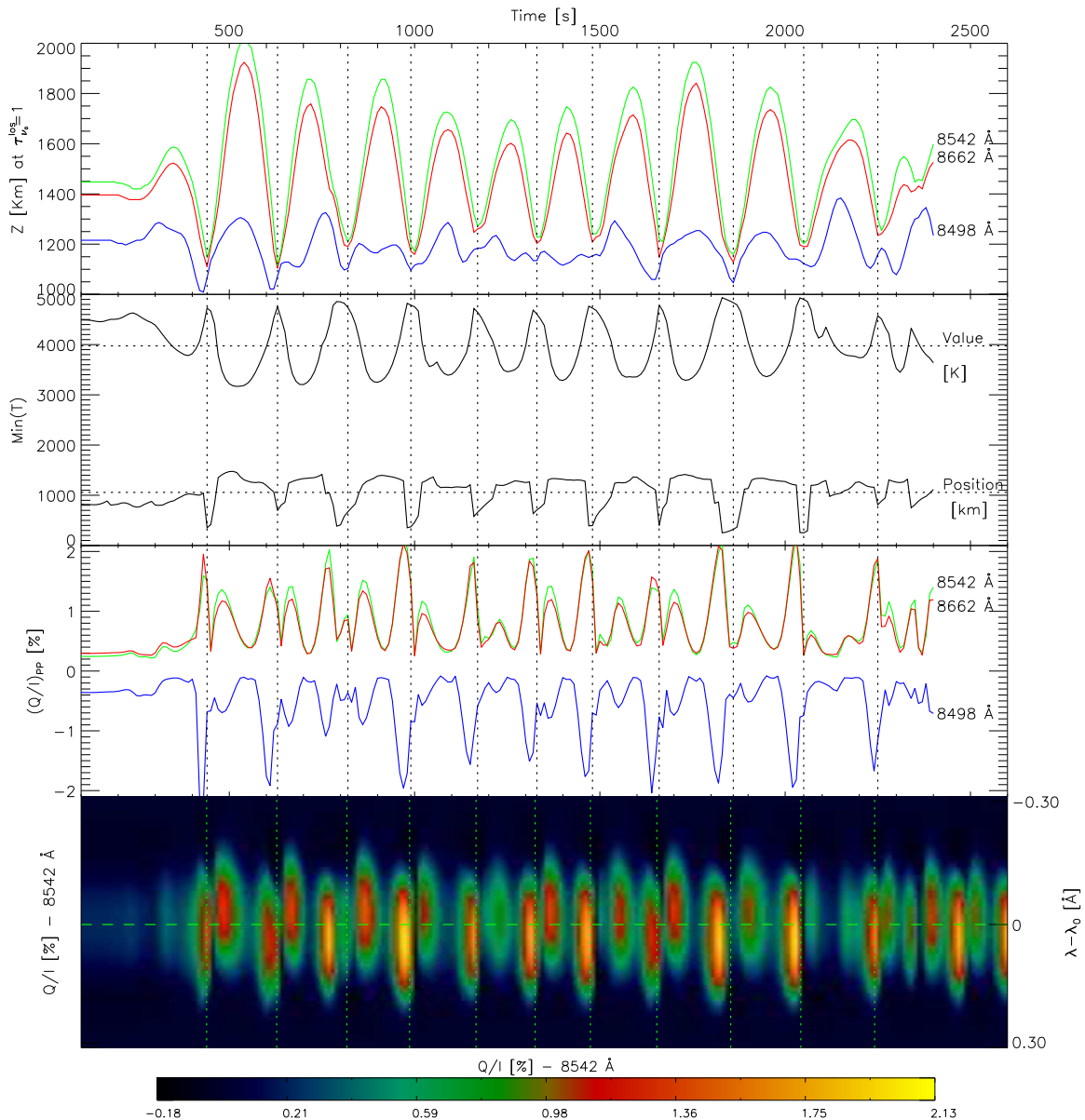


FIG. 1.— Top row: time evolution of the atmospheric heights where $\tau_{\nu_0}^{los} = 1$ for the three Ca II IR transitions. The dotted vertical lines are located at the local minimum of the $\tau_{\nu_0}^{los} = 1$ curve, and they can be considered to indicate the beginning and the end of each “three-minute” period with their corresponding expansion and compression phases. Second row: time evolution of the temperature value and atmospheric height of the temperature minimum. Third row: time evolution of the polarization contrast ($\max(Q/I) - \min(Q/I)$) for the three lines of the Ca II IR triplet. The polarization amplitude of the $\lambda 8498$ line has been multiplied by -5 to show the results for the three lines on the same scale. Note that, by definition, the line contrast is always positive, so with this quantity we cannot know if the polarization signal is positive or negative. Thus, with the artificial sign inversion done for the 8498 \AA line contrast in this figure, we try to illustrate that this line is the only one whose larger polarization amplitudes are negative. Bottom row: time evolution of the calculated $Q(\lambda)/I(\lambda)$ fractional linear polarization profile of the $\lambda 8542$ line.

wavelength and amplitude modulations are produced by the Doppler effect of the velocity gradients.

It is interesting to compare the mean Q/I amplitudes obtained in the hydrodynamical models with the one calculated in the FAL-C model. They differ notably (see horizontal lines in right panels of Fig. 2). In the 8542 \AA transition we have mean values around 1%, 0.31% and 0.42% for the HD models with velocities, the HD models at rest and static FALC models, respectively. The results of these figures have been obtained using an integration time of 1040 s (~ 17 minutes), the duration of the temporal interval shown in Fig. 2. Neglecting the effect

of the velocity gradients in the HD models, we see that the resulting temporally-averaged scattering polarization signals (which include the impact of the temperature and density shocks) are similar to the Q/I profiles computed in the static FAL-C semi-empirical model.

4.2. The combined effect of velocity and temperature on the linear polarization.

In Fig. 3 we display some relevant magnitudes for three different situations in the simulation. The first column corresponds to a *quiet* time-step, with no shocks, zero velocity and without any kind of amplifications (it

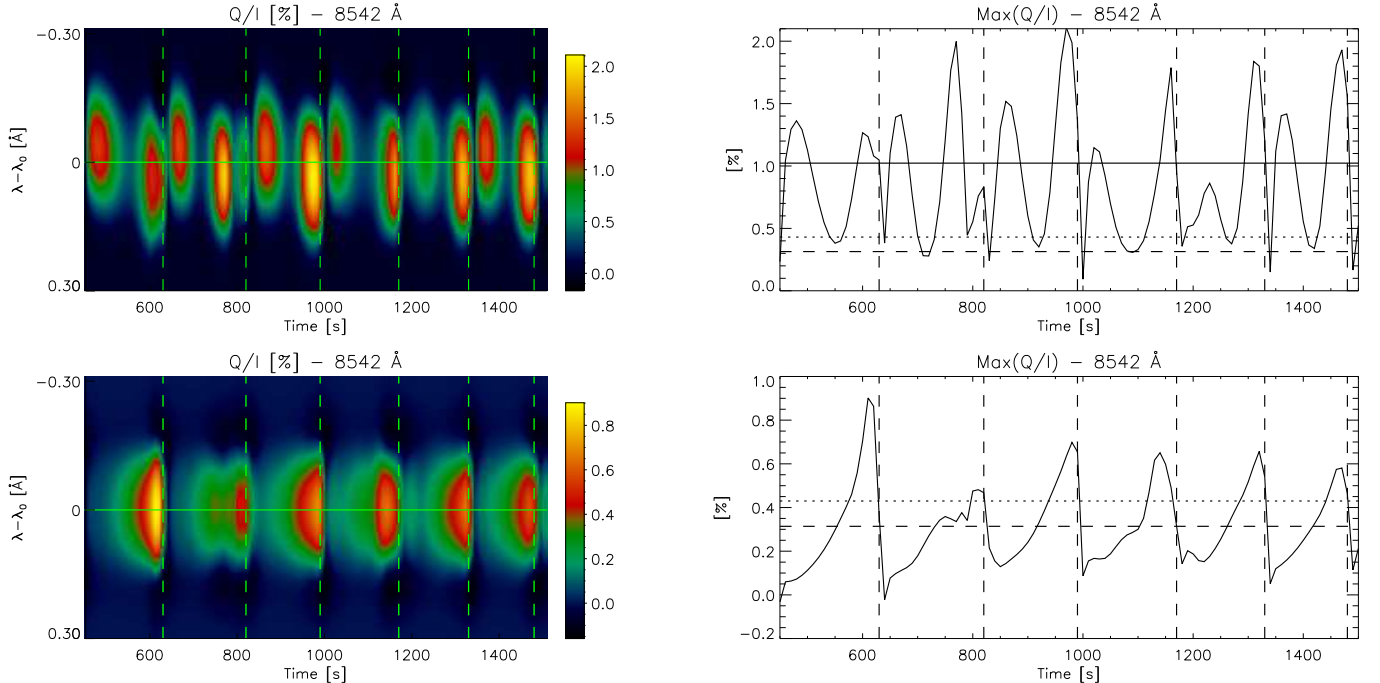


FIG. 2.— Temporal evolution of $Q(\lambda)/I(\lambda)$ (left column panels) and of the $\text{Max}(Q/I)$ peak amplitude (right column panels) during 1040 s (17 minutes) for the 8542 Å transition. The results of the upper panels take into account the effect of the velocity gradients, while those of the lower panels were obtained assuming zero macroscopic velocities while calculating the density-matrix elements. The vertical lines indicate the beginning and the end of each three-minutes period. The horizontal lines in the right column panels show the temporally-averaged amplitudes $\langle\langle Q\rangle\rangle/\langle\langle I\rangle\rangle$ obtained from the Q/I profiles computed in the strongly dynamic model, with the solid line indicating the polarization amplitude obtained when the effect of the velocity gradients is taken into account and the dashed lines showing the polarization amplitude obtained assuming zero macroscopic velocities. The dotted horizontal lines in the right panels indicate the polarization amplitudes obtained in the (static) FAL-C semi-empirical atmospheric model.

is the initial transient phase). The central column shows a phase of *compression*, in which shocks are important. Finally, the last column displays an *expansion* phase, in which the atmosphere is expanded and the shocks are already travelling over the transition region. Furthermore, we distinguish between the solutions when motions are taken into account (red lines) and the solutions obtained allowing shocks in all magnitudes but artificially setting the velocity to zero (black lines).

The normalized velocity $\xi_z = (\nu_0/c)v_z/\Delta\nu_D$, with $\Delta\nu_D$ the Doppler width of the absorption profiles (that depends on the temperature), c the speed of light and v_z the vertical velocity, is the quantity that controls the importance of the atmospheric motions in relation with the radiation anisotropy and the scattering polarization (see Paper I). Note that this quantity considers the combined effect of velocity and temperature. In the HD atmosphere models, ξ_z (solid lines in upper panels of Fig. 3) is only significant in the formation region of the IR triplet lines ($\tau_{\nu_0}^{los} \sim 1$ region with high velocity gradients, and not very high temperatures). Although shock waves increase the chromospheric temperature, the effect of the velocity gradients is predominant. The contrary occurs over the transition region, where the thermal line width is much larger than the Doppler shifts.

The expansion and contraction can be identified also in quantities such as the intensity source function and the Planck function (second row in Fig. 3). During contraction phases (middle column panels), high temperatures produce a more efficient population pumping towards upper levels, incrementing the emissivity and, consequently,

the source function. Additionally, during contraction the temperature shock occurs in optically thick and denser layers (deeper layers below $\tau_{\nu_0}^{los} = 1$), forcing the source function gradient to increase with respect to the static case at those heights. Note how in this last case the source function rises *as a whole* because of the warming (compare the source function in the middle panel, the black solid line that has been obtained neglecting velocities, with the non-dynamic source function in the left column). If the macroscopic velocity is now considered, we additionally get a jump in the source function (red lines in middle column of Fig. 3) caused by the velocity shock that is developed in this contraction phase. This behaviour is accompanied by a significant Doppler-induced anisotropy enhancement that amplifies the linear polarization, as shown in the corresponding lower panels of the same figure.

In the expansion phases, the shock waves move upward and the chromosphere becomes cooler. This induces a lower source function and smaller polarization amplitudes (as compared with the contraction phase). Otherwise, as the density of scatterers is now lower around the shock (because it moved upward to regions with $\tau_{\nu_0}^{los} < 1$), the temperature gradients have smaller effects on the polarization profiles than during the contraction phases. In this expansion time step, the black solid line representing the *static* source function is similar to the non-dynamic source function of the left column. However, once the motions are introduced, and despite of the fact that the shocks have already reached upper chromospheric layers, the remanent velocity field has still a siz-

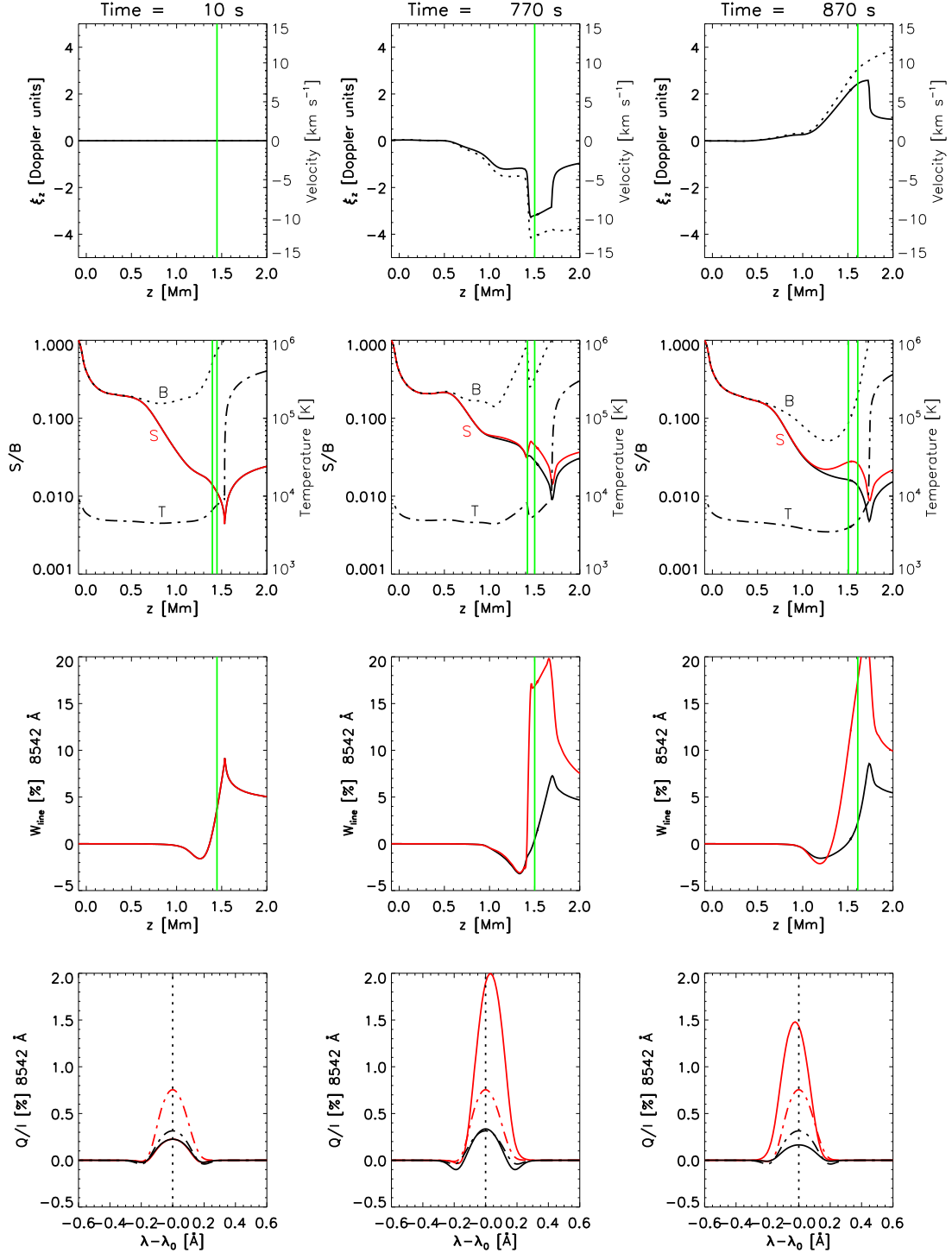


FIG. 3.— This figure shows the values of the quantities indicated in the vertical axes for the time steps 10 s. (left column, a ‘quiet’ situation), 770 s. (middle column, a compression stage) and 870 s. (right column, an expansion phase) of the strongly dynamic hydrodynamical simulation. First row (from top): macroscopic vertical velocity (dotted line) and dimensional vertical velocity ξ_z (solid line) versus height. The green line of each panel indicates the atmospheric height where $\tau_{\nu_0}^{los} = 1$. Second row (from top): temperature (dashed line), Planck function (dotted line), source function for the zero velocity approximation (solid black line) and source function allowing the influence of the model’s velocity gradients (red solid line). The green lines mark the instantaneous positions of $\tau_{\nu_0}^{los} = 1$ and $\tau_{\nu_0}^{los} = 2$. Third row (from top): line anisotropy factor (see equation 4 in Carlin et al. 2012) calculated for each of the above-mentioned cases; neglecting the effect of the velocity gradients (black solid line) or allowing it (red solid lines). Fourth row (from top): emergent Q/I profiles versus wavelength with respect to the line center, with the same color code than in previous panels. The dashed lines here are the time averages over the entire simulation, for each case (with or without velocities).

able gradient that enhances the source function (Doppler brightening effect).

4.3. Averaged values of the polarization profiles.

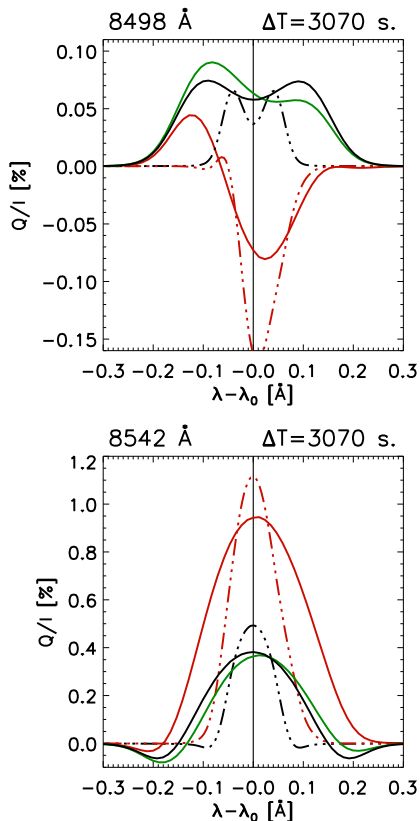


FIG. 4.— Fractional linear polarization profiles of the 8498 Å and 8542 Å lines after temporally averaging the Stokes I and Q profiles during 3070 seconds (51 minutes). These $\langle Q \rangle / \langle I \rangle$ profiles may be considered to emulate what can be actually observed with today’s solar telescopes. Black solid profiles: static case with $v_{\text{micro}} = 3.5 \text{ km s}^{-1}$. Red solid profiles: strongly dynamic case taking into account the effect of the velocity gradients and assuming $v_{\text{micro}} = 3.5 \text{ km s}^{-1}$. Black dashed profiles: strongly dynamic case neglecting the effect of the velocity gradients and assuming $v_{\text{micro}} = 0$. Red dashed profiles: strongly dynamic case taking into account the effect of the velocity gradients and assuming $v_{\text{micro}} = 0$. The green solid lines show the temporally averaged profiles obtained after applying the velocity free approximation (VFA) with $v_{\text{micro}} = 3.5 \text{ km s}^{-1}$ (i.e., neglecting the Doppler shifts of the macroscopic velocities when computing the density matrix elements, but taking them into account when calculating the emergent Stokes profiles).

In order to compute the average linear polarization signal that one would observe without any temporal resolution, we average Q and I (obtaining $\langle Q \rangle / \langle I \rangle$) over 3070 s (≈ 51 minutes) for four different cases (Fig. 4). We consider the cases with zero micro-turbulent velocity (dotted lines) and a constant micro-turbulent velocity of 3.5 km s^{-1} (solid lines). For each case, we distinguish between the results *switching off* the velocity (black lines) and the results allowing for macroscopic velocity fields (red lines).

When macroscopic motions are considered, the polarization profiles become asymmetric. Furthermore, they become more negative in the case of the 8498 Å transition and more positive in the other two transitions. The asymmetry of the red profiles is a consequence of the fact that, during the averaging period, the dynamical situations in which the velocity gradient is negative (velocity field mostly decreasing with height) dominate over the situations with velocity gradients that are mostly

positive. This predominance is not because the situations with negative velocity gradients are more frequent but because such situations are more efficient on amplifying the linear polarization. This happens during the compression phase because i) the velocity gradients are larger, ii) there is also a shock in temperature affecting the formation region and iii) the shock fronts are located just below the $\tau_{\nu_0}^{\text{los}} = 1$ height. The results are qualitatively the same independently of the micro-turbulent velocity value, but, when it is not considered, the amplification of $\langle Q \rangle / \langle I \rangle_{\text{pp}}$ is larger and the profiles are narrower.

If we decrease the averaging interval to 9 minutes, we obtain profiles that are essentially similar to the ones obtained by averaging during 51 minutes (showed in Fig. 4). If we integrate less than that, significant variations appear in the shape and amplitude of the emergent profiles. This indicates that, concerning the linear polarization, there is still reliable dynamic information contained in a time interval corresponding to a few 3-min cycles.

4.4. The velocity free approximation.

An approximation that is sometimes applied to solve radiative transfer problems in dynamical atmospheres (either taking into account the presence of atomic polarization or not) is the velocity free approximation (VFA). It is based on solving the SEE and RTE simultaneously but neglecting the effect of plasma motions. However, once they are consistently solved, such plasma motions are included in the synthesis of the emergent Stokes profiles (along $\mu = 0.1$ in our case). Consequently, the density matrix elements are calculated as if plasma motions did not affect them, reducing the complexity and computational effort of the problem since a reduced frequency grid is used to compute the mean intensity and the anisotropy. The results of applying it to each time step of our HD evolution is the temporal average illustrated as the green line in Fig. 4. This approximation is clearly not appropriate in our case, given that the profiles just become asymmetric (with respect to the static profiles) but without the amplification. The reason for this lack of amplification is that the anisotropy controlling the linear polarization is not correctly enhanced (see Paper 1). On the other hand, the asymmetry is purely due to the asymmetric absorption with respect to the line center that motions produce along the ray under consideration. Hence, in order to obtain reliable results it is mandatory to include the effect of Doppler shifts in the whole set of equations, and we conclude that the VFA should not be applied.

4.5. The effect of photospheric dynamics.

Given that the small velocity fields appearing in the photosphere are amplified because of the exponential decrease in the density while the perturbations travel outwards, the properties of the bottom boundary condition are determinant in the behaviour of the emergent Stokes parameter of chromospheric lines. We compare the strongly dynamic case that forms the core of our paper with the weakly dynamic case that has been already introduced in Sec. 3. Although the mean maximum velocity gradient is three times smaller in the weakly dynamic case and the averaged polarization amplitudes are also smaller than in the strongly dynamic one, we

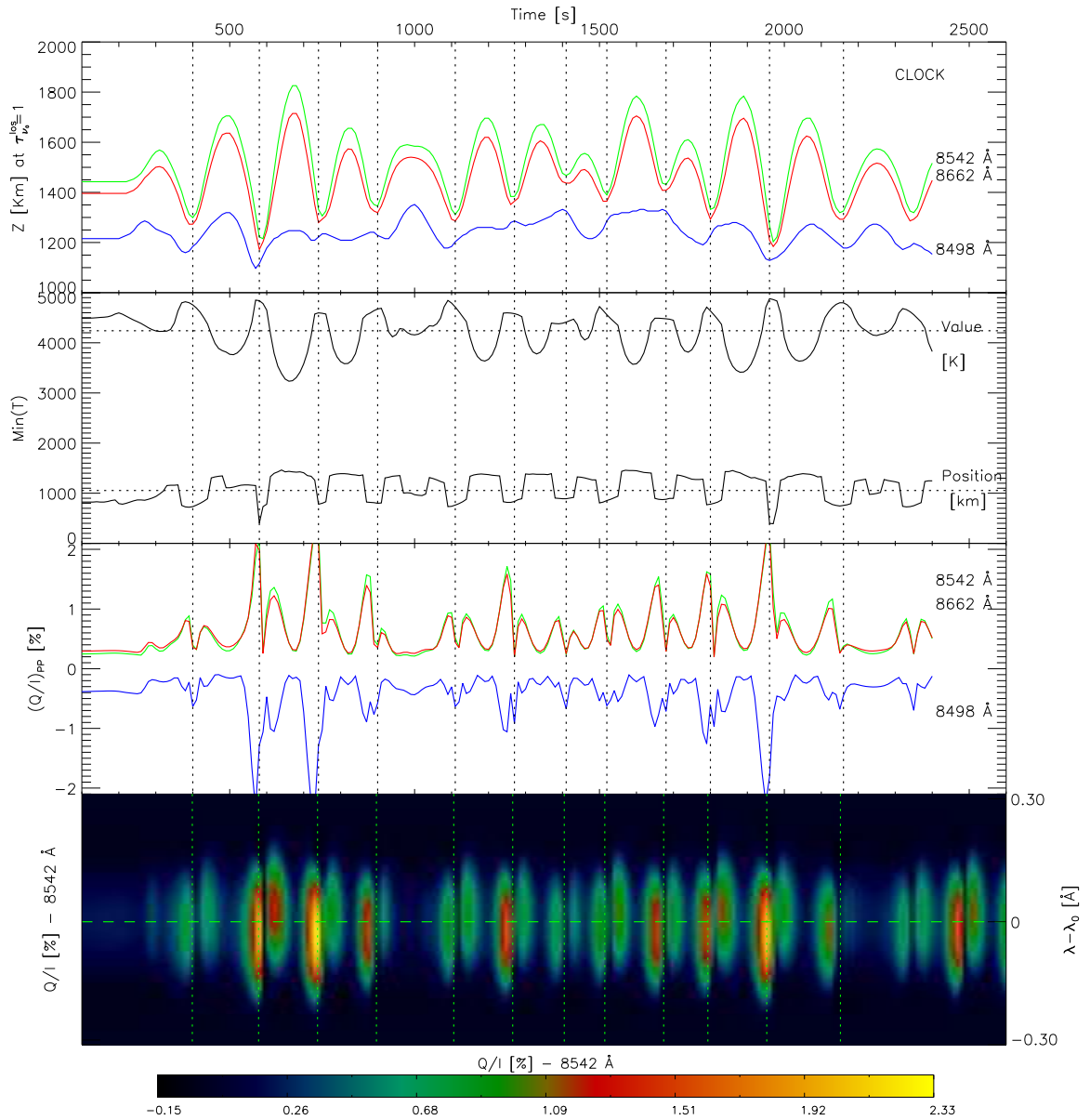


FIG. 5.— Same as Fig. 1, but for the weakly dynamic case. Remember that the blue line amplitude has been multiplied by -5 for scale reasons.

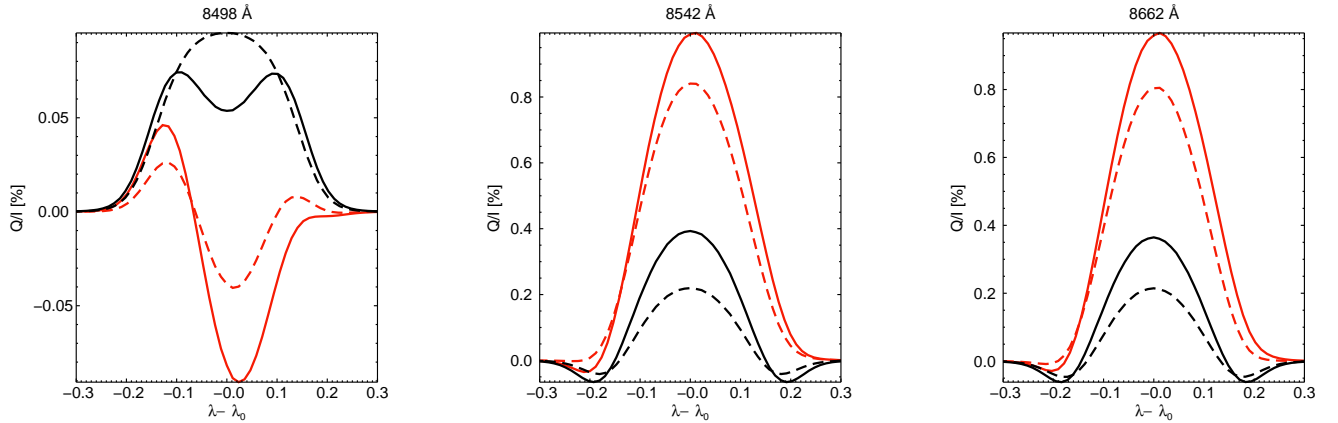


FIG. 6.— Comparison of the results in the strongly and weakly dynamic cases (see Sec. 4.5). All profiles are the resulting $\langle Q \rangle / \langle I \rangle$ profiles obtained averaging Q and I during 15 minutes of the considered simulation. Solid lines: results calculated in the strongly dynamic case. Dashed lines: results calculated in the weakly dynamic case. Black lines: results allowing variations in all magnitudes but neglecting the velocity. Red lines: results allowing the effect of the velocity gradients.

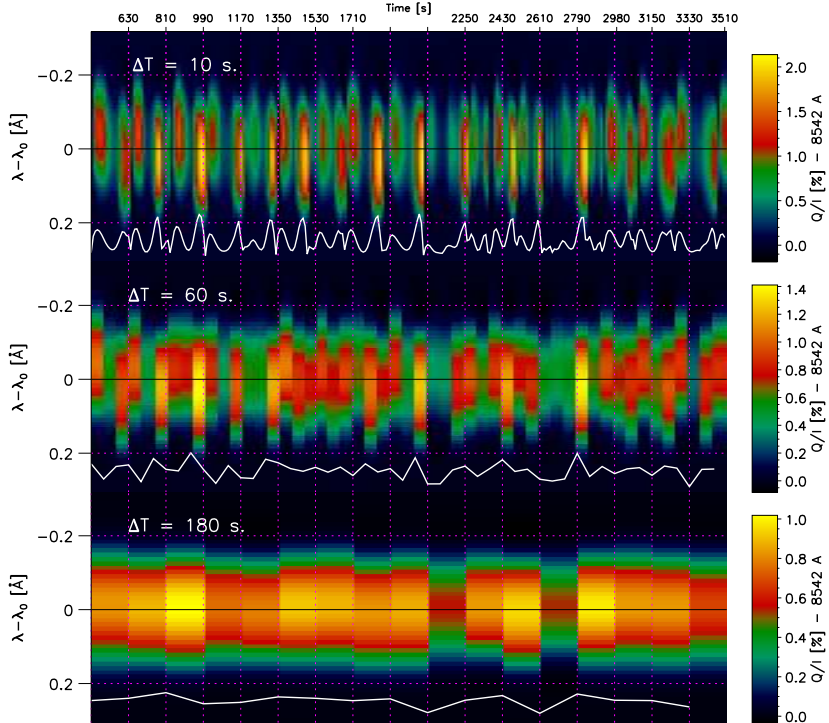


FIG. 7.— Temporal evolution of the emergent 8542\AA Q/I profiles for different integration times. Wavelength is in the vertical axis. From top to bottom we have a 10, 60 and 180 s. temporal resolution, respectively. The white solid lines show the temporal evolution of $(Q/I)_{pp}$ (i.e., the amplitude contrast at each time-step). Vertical dotted lines mark each three-minute period.

still find comparable or even slightly larger instantaneous $(Q/I)_{pp}$ amplitudes (see Fig. 5). The resulting averaged polarization profiles are qualitatively the same but they differ in amplitude (Fig. 6). This is a reasonable result because in the weakly dynamic scenario the instantaneous velocity gradients are smaller in general. Differences are especially critical for the 8498\AA line, whose linear polarization profiles can be positive, but also adopt significant negative values at redder wavelengths (when velocity gradients are mainly positive with height) or at bluer wavelengths (when velocity gradients are mainly negative with height). This behaviour produces cancel-

lation effects with integration times larger than a three-minute period. Furthermore, the central depression produced in the 8498\AA average profile when the velocity is neglected in the strongly dynamic simulation (solid black line in left panel of Fig. 6) do not appear in the average profile corresponding to the weakly dynamic case (dashed black line in the same panel) because of the differences in the instantaneous temperature stratifications. The sensitivity of this spectral line to the instantaneous photospheric perturbations and to the developed chromospheric shocks is larger than in the other two lines.

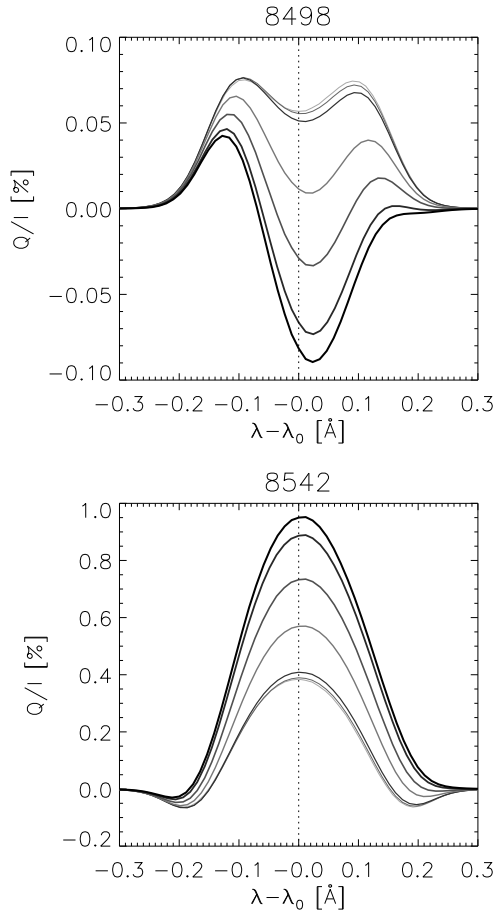


FIG. 8.— Resulting Q/I profiles after averaging Q and I during 15 minutes in the strongly dynamic simulation, using different values of F . F is the scaling factor by which we have multiplied the modulus of the macroscopic velocity at each atmospheric height. The curves correspond to $F = 1, 0.9, 0.7, 0.5, 0.2, 0.1, 0$, going from black colour (fully dynamic case) to lighter grey colour (static case). The results for the 8662 Å line are very similar to the ones obtained for the 8542 Å line.

4.6. The effect of the integration time.

In order to detect in the Sun the time evolution of the linear polarization signals, the observations must have enough time resolution, signal to noise ratio and spatial resolution. A sufficient spatial coherence is important to avoid cancellations of the contribution from different regions in the chromosphere evolving with different phases. If we consider the expected capabilities of the next generation of solar telescopes (like the European Solar Telescope, EST, or the Advanced Technology solar Telescope, ATST), we can aim at observing the emergent Stokes profiles of Fig. 7 with a 10 s cadence (upper panel)⁶. However, with the present telescopes and instrumentation, we are forced to integrate in time and/or space to detect the scattering polarization signals. If we degrade the temporal resolution of our results to an integration

⁶ Using EST (telescope diameter of 4 m, instrumental efficiency around 10%) and considering a spectral resolution of 30 mÅ, a spatial resolution of 0.1 arcsecs and an integration time of 1 s (ten times better than needed), it would be possible to observe the linear polarization of the 8542 Å line (line to continuum ratio of ~ 0.2) at the level of $Q/I \sim 10^{-3}$ with a confidence of 3σ over the noise.

time of 1 min (middle panel of Fig. 7) and 3 min (lower panel of Fig. 7) we clearly see that the time evolution becomes more difficult to detect. In the last case, the profiles are already so smoothed that the original features are completely lost, both in the spectral and temporal domains. The amplitude of the integrated signals are lower than in the original 10 s sequence by a factor of 2 (see the color scales). However, integration during time intervals ~ 1 min could reveal the amplification/modulation effect if we capture spectro-polarimetric signals similar to the ones showed in the middle row panel.

4.7. The effect of a decreasing velocity on the averaged profiles.

We also calculated what happens to the emergent averaged profiles in the strongly dynamic case (with 15 minutes of integration, emulating an observation) when we gradually reduce the velocity field by a constant scaling factor F , keeping the rest of atmospheric magnitudes unperturbed (see Fig. 8). As expected, we find that the polarization amplitudes decrease in proportion to F , from the original case, with $F = 1$, towards the static case, with $F = 0$. Note that the core of the 8498 Å line goes through zero for a certain F value (near $F = 0.6$). Thus, depending on the magnitude of the velocity gradients, its linear polarization amplitude will be positive or negative. This fact suggests an additional way to diagnose velocity gradients along the line-of-sight. However, it is important to keep in mind that this sensitivity also depends on the variations in density and temperature, as shown in Sec. 4.5.

Furthermore, the variation of the Q/I amplitudes is not linear with F . The change is small for small F , is larger for intermediate values of F , and again becomes smaller for the largest F , tending to saturation.

5. CONSIDERATIONS ON THE HANLE EFFECT

For magnetic field diagnostics with the Hanle effect it is often necessary to know the zero-field polarization reference (e.g., Stenflo 1994; Trujillo Bueno et al. 2004). That is what we have tried to do in previous sections, calculating and explaining the temporal evolution of the linear polarization profiles in chromospheric dynamic simulations. Ideally, this reference has to be computed under the same thermodynamical and dynamical conditions than in the real Sun but without magnetic field. As the Hanle effect often depolarizes the linear polarization signals, the difference between the observation and the zero-field calculation can be associated to a magnetic field by adjusting the magnetic field topology and intensity. The key point is that the reference amplitude must be as precise as possible. If it is imprecise, variations in the Stokes profiles can be associated to a magnetic field when they were really due to uncertainties in another magnitudes, like the temperature or the velocity field. Due to this reason, the fact that the solar chromosphere is a highly dynamic medium brings some complications for the use of the Hanle effect as a diagnostic mechanism.

A strategy to avoid the above-mentioned problem is known as the line ratio technique. It consists of finding a pair of spectral lines whose thermodynamical behaviour is identical but whose sensitivity to the magnetic field is different in some range of magnetic field intensity or inclinations (e.g., Stenflo et al. 1998;

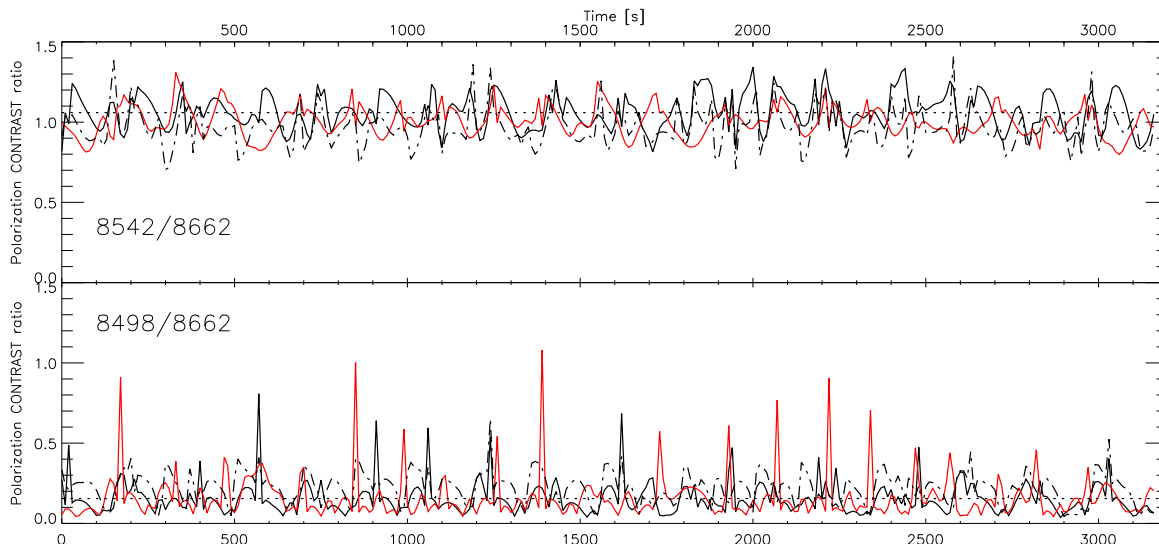


FIG. 9.— Black solid lines correspond to the strongly dynamic case. Red lines correspond to weakly dynamic case. Black dashed lines correspond to the strongly dynamic case but doing the calculations without micro-turbulent velocity. The line ratio $\varrho_3 = (Q/I)_{PP}^{8498} / (Q/I)_{PP}^{8542}$ is not shown because it is very similar to ϱ_1 and because can be obtained from the other two ratios.

Manso Sainz et al. 2004). In that case, the ratio between the polarization amplitudes should only change due to variations in the magnetic field, thus allowing us to measure it after a suitable calibration. As shown by Manso Sainz & Trujillo Bueno (2010), the main magnetic sensitivity difference among the lines of the Ca II IR triplet is between the $\lambda 8498$ line (which is sensitive to field strengths between 0.001 G and 10 G) and any of the $\lambda 8662$ and $\lambda 8542$ lines (which react mainly to sub-gauss magnetic fields and up to 10 G in the latter spectral line). Unfortunately, while the line-cores of the $\lambda 8662$ and $\lambda 8542$ lines originate in similar atmospheric layers, the $\lambda 8498$ line-core originates at significantly deeper atmospheric layers (see Figs. 1 and 5). Nevertheless, we have found useful to plot in Fig. 9 the time evolution of the following polarization line ratios:

$$\varrho_1 = \frac{(Q/I)_{PP}^{8498}}{(Q/I)_{PP}^{8662}}, \quad (1a)$$

$$\varrho_2 = \frac{(Q/I)_{PP}^{8542}}{(Q/I)_{PP}^{8662}}, \quad (1b)$$

where the super-index indicates the central wavelength of the transition in \AA . These quantities were calculated for each simulation considered before (weakly and strongly dynamic cases). The more stable they are, the more useful they will be for inferring the magnetic field.

We obtain that, in average, $\bar{\varrho}_1 = 0.15 \pm 0.10$ and $\bar{\varrho}_1 = 0.16 \pm 0.14$ for the strongly and weakly dynamic cases, respectively (lower panel in Fig. 9). The sudden shape variations (including maximum amplitudes passing by zero) of the 8498 \AA line induce large instantaneous excursions on ϱ_1 . As expected, a more stable line ratio is obtained for the second pair of transitions, which are precisely the ones that originate at similar chromospheric heights. We find $\bar{\varrho}_2 = 1.06 \pm 0.11$ and $\bar{\varrho}_2 = 1.00 \pm 0.09$ for the strongly and weakly dynamic cases, respectively (upper panel in Fig. 9). If we repeat the calculations setting to zero the micro-turbulent velocity in the strongly dynamic case we obtain $\bar{\varrho}_1 = 0.22 \pm 0.09$ and

$\bar{\varrho}_2 = 0.97 \pm 0.12$ (dashed black lines in Fig. 9). These results indicate that the $\bar{\varrho}_2$ line ratio shows a relatively stable behavior against variations of the velocity and temperature in the solar atmosphere. Consequently, in principle, ϱ_2 could be used as a suitable line ratio to estimate the magnetic field from spectropolarimetric observations of the $\lambda 8662$ and $\lambda 8542$ lines.

Regarding the sensitivity of these lines to the magnetic field and their applicability for the diagnostic of magnetic fields through the Hanle effect, several considerations have to be taken into account. First, the micro-turbulent velocity has a small influence on the averaged amplitudes and line ratios. Second, once the magnetic field is included in the calculations, the Hanle effect typically operates at the line center for static cases. However, in a dynamic situation there is not a preferred line center wavelength. As the maximum of the absorption and dispersion profiles occurs at different Doppler shifted wavelengths, the Hanle effect will operate in a small bandwidth around the line core. Third, according to the static calculations by Manso Sainz & Trujillo Bueno (2010), for chromospheric magnetic fields stronger than 0.1 G in the “quiet” Sun, the Q/I signal of the 8662 \AA line is expected to be Hanle saturated. Thus, variations between 0.1 and 10 G could be measured with ϱ_2 , being produced by changes in the linear polarization of the 8542 \AA line. Unfortunately, the fluctuations we see in Fig. 9 (exclusively due to the dynamics) have amplitudes of the same order of magnitude than those expected from the investigations of the Hanle effect in static model atmospheres (exclusively due to the magnetic field). More realistic results will be obtained when carrying out calculations of the Hanle effect of the Ca II IR triplet in dynamical model atmospheres. In any case, it is clear that for exploiting the polarization of these lines, we need instruments of high polarimetric sensitivity.

6. CONCLUSIONS

The results presented in this paper indicate that the vertical velocity gradients caused by the shock waves that take place at chromospheric heights in the HD models of

Carlsson & Stein (1997; 2002) have a significant influence on the computed scattering polarization profiles of the Ca II IR triplet. They show changes in the shape of the Q/I profiles of the three IR lines and clear enhancements in their amplitudes, as well as changes in the sign of the Q/I signal of the $\lambda 8498$ line. Interestingly enough, such modifications with respect to the static case are evident, not only in the temporally resolved Q/I profiles (e.g., see Fig. 2), but also in the temporally-averaged $\langle Q \rangle / \langle I \rangle$ profiles (e.g., see Fig. 4). This is true even with moderate macroscopic plasma velocities, simply due to the presence of strong vertical velocity gradients like the ones produced by shock waves. This may explain why the above-mentioned modifications of the scattering polarization profiles of the Ca II IR triplet are present not only in the strongly dynamic simulation (Carlsson & Stein 1997) but also in the weakly dynamic one (Carlsson & Stein 2002).

Our investigation points out that the development of diagnostic methods based on the Hanle effect in the Ca II IR triplet should take into account that the dynamical conditions of the solar chromosphere may have a significant impact on the emergent scattering polarization signals. This complication could be alleviated through the application of line ratio techniques. In Sec. 5 we have concluded that the ratio between the polarization amplitudes of the $\lambda 8542$ and $\lambda 8662$ transitions would be the best line-ratio choice. However, even in the absence of magnetic fields, the small fluctuations we see in the value of such a line ratio in dynamical model atmospheres could be confused with the presence of magnetic fields in the range between 0.1 and 10 G. Further work is necessary at this point.

In any case, the fact that realistic macroscopic velocity gradients may have a significant impact on the scattering polarization profiles of the Ca II IR triplet is interesting and important for the diagnostic of the solar chromosphere⁷. On the one hand, it provides a new observable for probing the dynamical conditions of the solar

chromosphere (e.g., by confronting observed Stokes profiles with those computed in dynamical models). On the other hand, the exploration of the magnetism of the quiet solar chromosphere via the Hanle effect in the Ca II IR triplet (either through the forward modeling approach or via foreseeable Stokes inversion approaches) would have to be accomplished without neglecting the possible effect of the atmospheric velocity gradients on the atomic level polarization.

Several points are still unanswered after this work. First, we need to investigate the sensitivity to the Hanle effect of the Q/I and U/I profiles of the Ca II IR triplet using magnetized and dynamical atmospheric models. Second, we have to investigate whether our one-dimensional radiative transfer results remain valid after considering realistic three-dimensional models, such as those resulting from magneto-hydrodynamical simulations (e.g. Wedemeyer et al. 2004; Leenaarts et al. 2009). We would tentatively expect that the strong stratification that gravity imposes in the solar atmosphere facilitate shocks that propagate mainly in the vertical direction, but with a reduced strength, given the increased degrees of freedom.

Finally, we mention that our results could be of potential interest in other astrophysical contexts. For instance, the mechanism of polarization enhancement due to the presence of shocks might well be the explanation for the changing amplitudes of the linear polarization signals reported in variable pulsating Mira stars (Fabas et al. 2011).

We are grateful to Rafael Manso Sainz (IAC) for several useful discussions and advice with the radiative transfer computations. Financial support by the Spanish Ministry of Economy and Competitiveness through projects AYA2010-18029 (Solar Magnetism and Astrophysical Spectropolarimetry) and CONSOLIDER INGENIO CSD2009-00038 (Molecular Astrophysics: The Herschel and Alma Era) is gratefully acknowledged.

REFERENCES

- Carlin, E. S., Manso Sainz, R., Asensio Ramos, A., & Trujillo Bueno, J. 2012, *ApJ*, 751, 5
- Carlsson, M., & Stein, R. F. 1997, *ApJ*, 481, 500
- Carlsson, M., & Stein, R. F. 2002, in *SOHO-11: From Solar Minimum to Maximum*, ed. A. Wilson (ESA SP-508; Noordwijk: ESA), in press
- Casini, R., & Landi Degl'Innocenti, E. 2007, in *Plasma Polarization Spectroscopy*, ed. T. Fujimoto & A. Iwamae (Heidelberg:Springer), 247
- De la Cruz Rodríguez, J., Socas-Navarro, H., Carlsson, M., & Leenaarts, J. 2012, *Astronomy and Astrophysics*, 543, 34
- Fabas, N., Lèbre, A., & Gillet, D. 2011, *A&A*, 535, A12
- Harvey, J. 2009, in *Solar Polarization 5*, ed. S. Berdyugina, K. Nagendra, & R. Ramelli, ASP Conference Series (San Francisco: Astronomical Society of the Pacific), 157
- Kurucz, R. L., Furenlid, I., Brault, J., & Testerman, L. 1984, *Solar flux atlas from 296 to 1300 nm*
- Landi Degl'Innocenti, E., & Landolfi, M. 2004, *Polarization in Spectral Lines* (Kluwer Academic Publishers)
- Leenaarts, J., Carlsson, M., Hansteen, V., & Rouppe van der Voort, L. 2009, *ApJL*, 694, L128
- Manso Sainz, R., Landi Degl'Innocenti, E., & Trujillo Bueno, J. 2004, *ApJL*, 614, L89
- Manso Sainz, R., & Trujillo Bueno, J. 2003a, *Physical Review Letters*, 91, 111102
- Manso Sainz, R., & Trujillo Bueno, J. 2003b, in *Astronomical Society of the Pacific Conference Series*, Vol. 307, *Solar Polarization*, ed. J. Trujillo-Bueno & J. Sanchez Almeida, 251
- . 2010, *ApJ*, 722, 1416
- Parker, E. N. 2007, *Conversations on Electric and Magnetic Fields in the Cosmos* (Princeton University Press)
- Stenflo, J. O. 1994, *Solar Magnetic Fields. Polarized Radiation Diagnostics* (Dordrecht: Kluwer Academic Publishers)
- Stenflo, J. O., Keller, C. U., & Gandorfer, A. 1998, *A&A*, 329, 319
- . 2000, *A&A*, 355, 789
- Trujillo Bueno, J. 2001, in *ASP Conf. Ser. 236: Advanced Solar Polarimetry – Theory, Observation, and Instrumentation*, ed. M. Sigwarth, 161
- Trujillo Bueno, J. 2010, in *Magnetic Coupling between the Interior and Atmosphere of the Sun*, ed. S. Hasan & R. Rutten (Berlin Heidelberg: Springer-Verlag), 118
- Trujillo Bueno, J., Shchukina, N., & Asensio Ramos, A. 2004, *Nature*, 430, 326
- Wedemeyer, S., Freytag, B., Steffen, M., Ludwig, H.-G., & Holweger, H. 2004, *A&A*, 414, 1121

⁷ The physical mechanism is general, but its observable effects are expected to be significantly less important in broader spectral

lines, such as the Ca II K line and Ly α .